Applied Physics Reviews

RESEARCH ARTICLE | JANUARY 24 2024

Crystal-liquid duality driven ultralow two-channel thermal conductivity in α-MgAgSb FREE

Jingyu Li ; Xiyang Li ; Yongsheng Zhang ; Jianbo Zhu ; Enyue Zhao ; Maiko Kofu ; Kenji Nakajima ; Maxim Avdeev ; Peng-Fei Liu ; Jiehe Sui ; Huaizhou Zhao ; Fangwei Wang ; Junrong Zhang

Appl. Phys. Rev. 11, 011406 (2024)
https://doi.org/10.1063/5.0173680

Applied Physics Reviews ARTICLE pubs.aip.org/aip/are

Crystal-liquid duality driven ultralow two-channel thermal conductivity in -MgAgSb

Cite as: Appl. Phys. Rev. **11**, 011406 (2024); doi: 10.1063/5.0173680
Submitted: 23 August 2023 · Accepted: 26 December 2023 ·
Published Online: 24 January 2024

View Online Export Citation CrossMark

Jingyu Li,[1,2] Xiyang Li,[3,a)] Yongsheng Zhang,[4] Jianbo Zhu,[5] Enyue Zhao,[6] Maiko Kofu,[7] Kenji Nakajima,[7] Maxim Avdeev,[8] Peng-Fei Liu,[1,2,b)] Jiehe Sui,[5] Huaizhou Zhao,[3] Fangwei Wang,[3,6,b)] and Junrong Zhang[1,2,b)]

AFFILIATIONS

[1]Institute of High Energy Physics, Chinese Academy of Sciences, Beijing 100049, China
[2]Spallation Neutron Source Science Center, Dongguan 523803, China
[3]Beijing National Laboratory for Condensed Matter Physics, Institute of Physics, Chinese Academy of Sciences, Beijing 100190, China
[4]Advanced Research Institute of Multidisciplinary Sciences, Qufu Normal University, Qufu, Shandong Province, 273165, China
[5]State Key Laboratory of Advanced Welding and Joining, Harbin Institute of Technology, Harbin 150001, China
[6]Songshan Lake Materials Laboratory, Dongguan 523808, China
[7]Japan Proton Accelerator Research Complex, Japan Atomic Energy Agency, Tokai, Ibaraki 319-1195, Japan
[8]Australian Nuclear Science and Technology Organisation, Lucas Heights, NSW 2234, Australia

[a)]**Present address:** Department of Physics & Astronomy and Stewart Blusson Quantum Matter Institute, University of British Columbia; Vancouver V6T1Z4, Canada
[b)]**Authors to whom correspondence should be addressed:** pfliu@ihep.ac.cn; fwwang@iphy.ac.cn; and jrzhang@ihep.ac.cn

ABSTRACT

The desire for intrinsically low lattice thermal conductivity (κ_L) in thermoelectrics motivates numerous efforts on understanding the microscopic mechanisms of heat transport in solids. Here, based on theoretical calculations, we demonstrate that α-MgAgSb hosts low-energy localized phonon bands and avoided crossing of the rattler modes, which coincides with the inelastic neutron scattering result. Using the two-channel lattice dynamical approach, we find, besides the conventional contribution (∼70% at 300 K) from particlelike phonons propagating, the coherence contribution dominated by the wavelike tunneling of phonons accounts for ∼30% of the total κ_L at 300 K. By considering dual contributions, our calculated room-temperature κ_L of 0.64 W m^{-1} K^{-1} well agrees with the experimental value of 0.63 W m^{-1} K^{-1}. More importantly, our computations give a nonstandard $\kappa_L \propto T^{-0.61}$ dependence, perfectly explaining the abnormal temperature-trend of $\sim T^{-0.57}$ in experiment for α-MgAgSb. By molecular dynamics simulation, we reveal that the structure simultaneously has soft crystalline sublattices with the metavalent bonding and fluctuating liquid-like sublattices with thermally induced large amplitude vibrations. These diverse forms of chemical bonding arouse mixed part-crystal part-liquid state, scatter strongly heat-carrying phonons, and finally produce extremely low κ_L. The fundamental research from this study will accelerate the design of ultralow-κ_L materials for energy-conversion applications.

I. INTRODUCTION

Low lattice thermal conductivity (κ_L) is essential for developing high-performance thermoelectric materials for energy conversion,[1,2] as well as for designing efficient thermal management systems in electronic devices.[3,4] Naturally, numerous efforts on phonon blocking engineering,[5–7] such as all-scale hierarchical architectures,[8] enhancing atomic ordering,[9] high-entropy engineering,[10] and solid solution alloying,[11,12] have been devoted to reducing the κ_L of materials for boosting the thermoelectric figure of merit.[13] However, these methods introduce scattering of the charge carriers and strongly reduce the electrical transport.[14] Alternatively, seeking solids with intrinsically low κ_L, including complex crystal structures (e.g., skutterudites[15] or clathrates[16]) liquid-like materials with structural disorders,[17,18] as well as strongly anharmonic materials,[19–22] has gained popularity because they offer the only independent control among transport carriers for pursuing high thermoelectric performance.[5–7,13,23] In particular, it is of great importance to understand the correlation among bonding nature, lattice dynamics, and heat propagation in these intrinsic ultralow-κ_L solids.[24]

α-MgAgSb, with high thermoelectric performance, shows great potential as candidates for near-room temperature power

generation.[25–36] It achieves a high figure of merit of ∼1.4 at 525 K,[31] along with experimental demonstration of a record high conversion efficiency of ∼8.5% between 293 and 518 K under single thermoelectric leg operating.[26] Recently, using MgCuSb[37] as a thermoelectric interface material, the MgAgSb/$Mg_{3.2}Bi_{1.5}Sb_{0.5}$ module exhibits a record-breaking conversion efficiency of ∼9.25% at 300 K.[38] Clearly, α-MgAgSb holds such superb performance because of its relatively high power factor in combination with the ultralow κ_L.[27] In our previous work, we roughly attribute its ultralow κ_L to the static local structure distortion and strong phonon anharmonicity.[39] By solving the Boltzmann transport equation, our calculated temperature dependence is $\kappa_L \propto T^{-1.02}$, which is badly deviated from the experiment tendency of $\sim T^{-0.57}$ due to the result solely based on harmonic approximations and three-phonon scattering.[39,40] It is both scientifically and technologically significant to understand the physics of heat transport in α-MgAgSb with more precise means beyond the conventional anharmonicity being included.

Herein, we use first-principles Wigner formulation of two-channel thermal transport to unravel the relationship between the phonon dynamics and abnormal temperature-dependence low-κ_L behavior of α-MgAgSb. By combining inelastic neutron scattering (INS) experiments with calculations, we demonstrate the presence of low-energy localized phonon bands and avoided crossings of rattling modes in α-MgAgSb, which originate from loosely bonded atoms exhibiting thermally induced large amplitude vibrations. By capturing both the conventional particlelike and wavelike behaviors of phonons, our calculated κ_L aligns remarkably well with the measured results in terms of values and temperature dependence. The analysis point to the hierarchical bonds driven crystal-liquid duality as the underlying causes that lead to the suppression of heat conduction in α-MgAgSb.

II. EXPERIMENTAL AND THEORETICAL PHONONS

α-MgAgSb crystallizes in the body-centered tetragonal space group of $I\bar{4}C2$ (No. 120). In Fig. S1, the structure exhibits distorted MgSb rock salt sublattices, rotated by 45 degrees around the *c*-axis with respect to the unit cell. Ag atoms occupy half of the Mg-Sb pseudocubes. There are one independent Mg atom in 16*i* and one Sb atom in 16*i* Wyckoff positions, while Ag atoms have three inequivalent sites of 4*a*, 4 *b*, and 8*e* for Ag1, Ag2, and Ag3, respectively. The details of highly consistent optimized and experimental parameters are shown in Table S1. We first study lattice dynamics of α-MgAgSb by the orientation-averaged dynamic structure factor S(**Q**,E) with INS on powder sample. As shown in Fig. 1(a), it reveals a strong scattering pattern originating from the quasi-Brillouin-zone center at $\mathbf{Q} = 2.8$ Å^{-1}, which reaches its maximum at about 4 meV with excess low-energy modes. Using Euphonic,[41] first-principles computed S(**Q**,E) is plotted in Fig. 1(b), showing excellent agreement in terms of both the position and intensity in the heat map with the INS data in Fig. 1(a).

To rationally assign the strong low-energy modes in Fig. 1(a), we calculate S(**Q**,E)-weighted phonon dispersion in the first Brillouin (000) zone at 300 K, using the same parameters in Fig. 1(b) with Euphonic.[41] As the high-resolution neutron diffraction data shows two

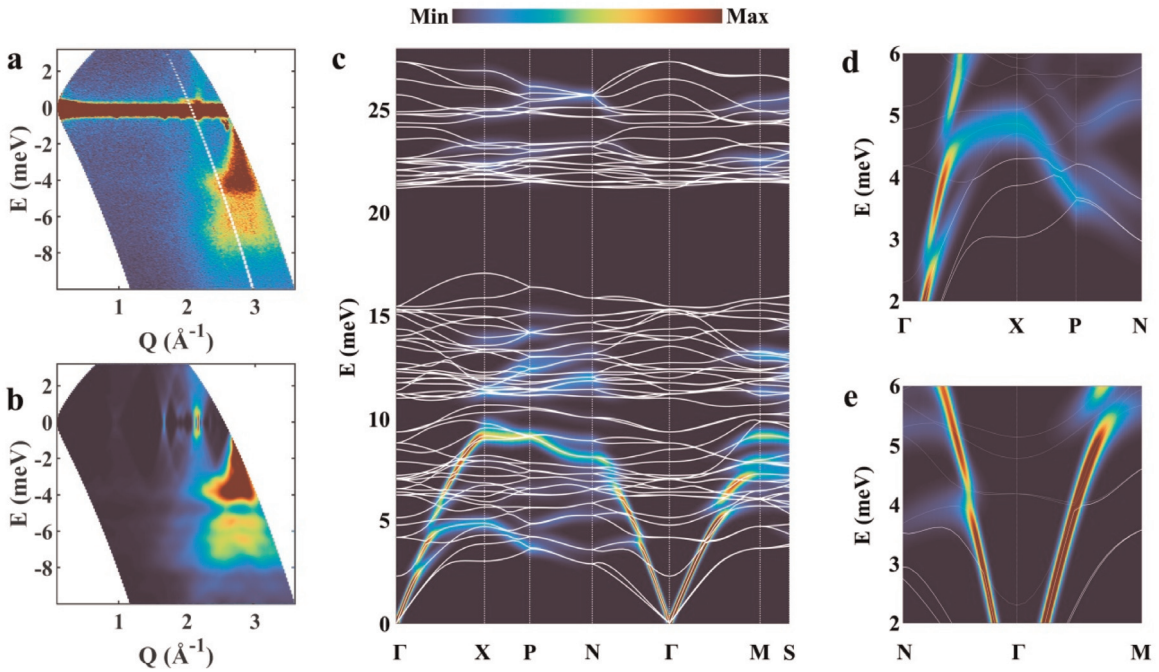

FIG. 1. Experimental and calculated phonons of α-MgAgSb. (a) The contour plot of the dynamic structure factor S(**Q**,E) obtained by inelastic neutron scattering with an incident neutron energy of $E_i = 4.68$ meV at 300 K from AMATERAS measurements. (b) Corresponding powder-averaged coherent S(**Q**,E) at 300 K generated by the renormalized force constant matrix output via first-principles calculations with the Euphonic package.[40] (c) Corresponding S(**Q**,E) weighted phonon dispersion relationship at 300 K calculated with Euphonic in the first Brillouin zone. The color saturation increases linearly from zero to the maximum value. [(d) and (e)] Enlarged views of avoided-crossing modes in S(**Q**,E) weighted phonon dispersion in Fig. 1(c) with energy ranging from 2 to 6 meV.

strongest peaks of (400) and (224) at $\mathbf{Q} = 2.8\ \text{Å}^{-1}$ in Fig. S2, we also calculate S(**Q**,E)-weighted spectra for the Brillouin zones centered at the (400) and (224) Bragg peaks, respectively, which may guide the potential single-crystal INS experiment in the future.[21] In Figs. 1(c) and S3, in addition to acoustic vibrations starting from the Γ point, it shows several nearly flat and intense optical phonon bands below 5.0 meV dominant in the momentum space. These causes strong phonon density of states (DOS) in the vicinity of about 4 meV at $\mathbf{Q} = 2.8\ \text{Å}^{-1}$ in Figs. 1(a) and 1(b). In the range from 5.0 to 10.0 meV, there are some optical phonon bands standing out with bright colors. From the 10.0 to 28.0 meV energy region, only some flat optical branches are observed weakly. The overall characteristics are captured by INS with the larger incident neutron energy of $E_i = 42.00$ meV in Fig. S4.

In the previous work only based on the powder INS study,[39] it is discovered that the compound's intrinsic distorted rock salt sublattice scatters nearly all transverse acoustic phonons. However, the simulation presented here in Fig. S3 reveals that there are abundant phonon DOS from the transverse acoustic phonons in both the (400) and (224) zones. It should be noted that the powder INS data provides an average DOS over various directions, while the data depicted in Figs. 1(c) and S3 only corresponds to specific directions and zones. These require further confirmation through INS measurements on single crystals. Beyond these, we see there are low-energy optical branches, which strongly overlap with the acoustic branches. This is in general, accompanied by avoiding the crossing of acoustical and optical branches with the presence of the concerted rattling modes.[42] To see it clearly, we zoom in of Fig. 1(c) on the low-energy range from 2 to 6 meV of the S(**Q**,E)-weighted phonon dispersion in the first Brillouin zone. In Figs. 1(d) and 1(e), undoubtedly, α-MgAgSb has avoided crossings of optical and acoustic phonon branches.

The avoided-crossing behavior, which has previously been proposed in clathrates and filled skutterudites,[15,16,42] has been ascribed to the independent rattling motions of fluctuating atoms. These rattling motions are incoherent localized modes, which can be well described by the localized Einstein modes observed by the powder INS and heat capacity measurements.[42–45] To see it in α-MgAgSb, the generalized phonon density of states (GDOS) are calculated by integrating results of $\left[1 - e^{-\frac{E}{k_B T}}\right] \frac{E}{Q^2} S(\mathbf{Q}, E)$, where $\left[1 - e^{-\frac{E}{k_B T}}\right]$ means the Bose–Einstein statistics, k_B is the Boltzmann constant, and T is the temperature. Figure 2(a) shows the experimental GDOS with an integration **Q** region of 1.0–3.0 Å at 300, 385, and 485 K, respectively, by INS. There exist obviously weak temperature-dependent low-energy Einstein modes around 4.0 meV, resulting in strong patterns in Fig. 1(a), which coincides with the low-temperature heat capacity measurements by fitting the Debye–Einstein model in the previous work.[35,46] On the basis of the renormalized force constant from molecular dynamics, we calculate GDOS at 300, 400, and 500 K in Fig. 2(b). They exhibit the same feature of strong low-energy peak at ∼3.5 meV in consistent with the experiment (at around 4.0 meV) by INS. By resolving atom-decomposed GDOS, we see the phonon modes from 0 to 10 meV mainly derive from the collective motions of Ag atoms in Fig. 2(c). In the range of 10–18 meV, the vibrations of Mg and Sb atoms mainly contribute to the phonon DOS. For high-energy optical phonons from 18 to 28 meV, they are mainly from Mg atoms. From the above, we conclude the low-energy Einstein modes are caused by the Ag atoms, particularly rattling movements of Ag1 atoms in Fig. 2(d). From the

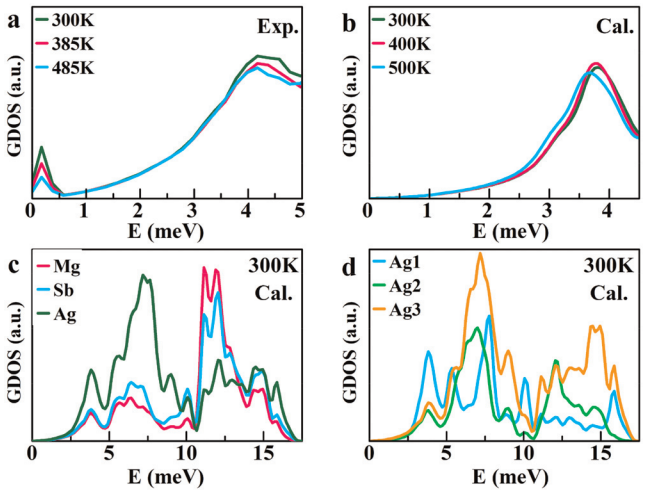

FIG. 2. Low-energy Einstein modes in α-MgAgSb. (a) Neutron-weighted phonon density of states measured by high-resolution INS in α-MgAgSb at 300, 385, and 485 K, respectively. (b) Calculated low-energy neutron-weighted phonon density of states for α-MgAgSb at 300, 400, and 500 K based on the renormalized harmonic force constants from molecular dynamics. (c) Calculated atom-decomposed GDOS at 300 K for Mg, Sb, and Ag atoms, respectively. (d) The enlarged atom-decomposed GDOS for three Ag atoms at 300 K. The units of phonon DOS are arbitrary.

finite-temperature phonon spectra in Fig. S5, same as shown in Fig. 1, low-energy optical modes strongly overlap with acoustical phonons. Specifically, both acoustic and optical phonon modes show up at about 4 meV with excess GDOS by INS in Fig. 2(a). These can greatly suppress the phonon group velocity and phonon lifetimes, which accordingly lower the κ_L. In addition, the lowest optical mode has the energy of 1.93 meV (15.57 cm^{-1}, 0.47 THz) at the Γ point. This value is quite small due to the oscillator of the heavy atoms, as previously reported.[46] Upon heating, the lowest-energy optical mode at Γ slightly harden, along with weak temperature-independent low-energy Einstein modes in Fig. 2(a).

III. CRYSTAL-LIQUID DUALITY

As discussed above, there are low-energy Einstein modes with the suppressed group velocity. These soft vibrations are usually associated with weakly bound atoms that randomly fluctuate as rattlers with ultra-large atom displacement parameters (ADPs). In α-MgAgSb, the ADPs of atoms at 300 K are 0.009, 0.013, 0.047, 0.012, and 0.013 in Fig. S6, for Mg, Sb, Ag1, Ag2, and Ag3, respectively, extracted by the Rietveld refinement method.[47] Large ADPs of Ag1 atoms indicate that they are weakly bonded in the lattice, which will induce partially liquid-like motions[48] as melted sublattice in α-MgAgSb. These variable values are together with the existence of hierarchical chemical bonds.[46] As an evidence, we calculate the shared and transferred charges in α-MgAgSb and find it holds the well-established metavalent bonds[49] alongside many known low-κ_L materials[49–52] in Fig. S7. Meanwhile we calculate the velocity autocorrelation function (VACF) as a function of time from molecular dynamics (MD) simulations in Figs. 3(a) and S8. The VACFs of Mg and Sb atoms are oscillatorily damped as in solids. The first valley of Ag1 atoms is widely distributed and rapidly damps as time grows as in liquids where one single-valley minimum is present,[48] while the VACFs of Ag2 and

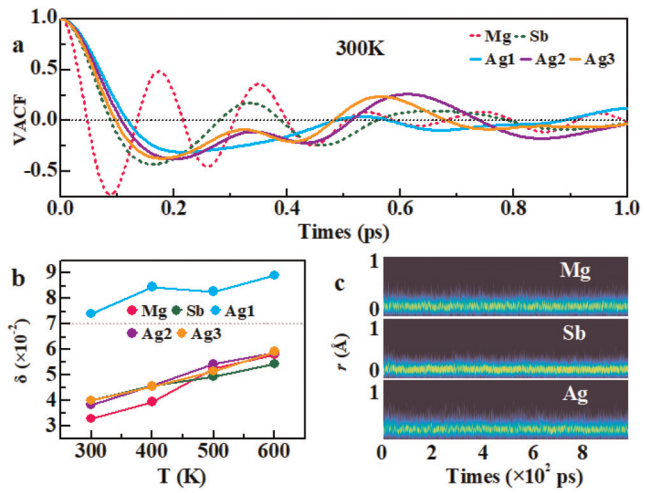

FIG. 3. Liquid-like motions in α-MgAgSb. (a) The decay patterns of the velocity autocorrelation function for different atoms in α-MgAgSb from molecular dynamics simulations at 300 K. (b) Lindemann parameters (δ) for Mg, Ag, and Sb atoms in α-MgAgSb at 300, 400, 500, and 600 K, respectively. (c) Calculated self-part of van Hove correlation functions at 300 K for Mg, Ag, and Sb atoms, respectively. The ordinate represents the range of atomic fluctuations as a function of time.

Ag3 atoms first undergo the double-potential-well valley and then weaken in oscillating. These features indicate Ag atoms exhibit partially liquid-like motions in α-MgAgSb under finite temperatures and the compound holds the crystal-liquid duality,[48,50–53] which contains both the crystalline framework and noncrystalline rattling atoms with large-amplitude random movements.

To validate the above feature, we calculate the Lindemann parameter δ of atoms in α-MgAgSb, by $\delta = \mathrm{ADP}^{1/2}/R_{\mathrm{NN}}$, where R_{NN} is the nearest-neighbor distance. The δ at 300 K are 0.033, 0.040, 0.074, 0.038, and 0.040 for Mg, Sb, Ag1, Ag2, and Ag3, respectively, in Fig. 3(b). The value of Ag1 atom exceeds the criterion of melting (≥0.07) as in liquids,[54] while other atoms are normal for crystals. As shown in Figs. 3(c) and S9, the self-part of the van Hove correlation function $G_s(r, t)$,[55] calculated from the MD simulations, illustrates the probability that a particle will diffuse away from its initial positions by a distance r after a period t. As time grows, it fluctuates nearly around a fixed value for each atom. There is no jump diffusion for all atoms in α-MgAgSb, which is different from superionic thermoelectric $AgCrSe_2$[56] with the existence of quasi-2D liquid-like diffusion. It is also verified by the simulated trajectory of atoms of α-MgAgSb at 400 and 500 K from MD in Figs. S8(c) and S8(d) with all atoms being constrained to around their equilibrium positions. Thus, Ag1 atoms in α-MgAgSb have large oscillation amplitude with partially fluid-like diffusions but act as rattlers restricted to their positions (like fillers in skutterudites[15]). α-MgAgSb has the mixed crystal-liquid state with the well-ordered structure, which deviates from the crystalline picture of the classical solids. This trait is different from the well-known liquid-like materials that hold structural disorders, such as $AgCrSe_2$,[57] Cu_2Se,[18] and argyrodites.[58]

IV. THERMAL TRANSPORT MECHANISM

As described above, α-MgAgSb has the crystal-liquid hybrid state. In addition, it is experimentally reported to hold an ultralow κ_L of ~0.63 $\mathrm{W\,m^{-1}\,K^{-1}}$ at 300 K (Refs. 35 and 39) and nonstandard temperature dependence of $\sim T^{-0.57}$ in Fig. S10. To accurately describe the mechanism of heat transfer, we calculate the κ_L of α-MgAgSb in the framework of the Wigner transport equation which physically comprises two-channel thermal components: crystal-like (population conductivity from particlelike phonon propagation, κ_p) and liquid-like (coherence conductivity from wavelike phonon tunneling, κ_c) terms: $\kappa_L = \kappa_p + \kappa_c$, where κ_p coincides with the standard Peierls–Boltzmann thermal conductivity in crystals from particlelike phonons, while the wavelike phonon tunneling contributes to κ_c as described by the Allen–Feldman equation for amorphous materials.

Clearly, Fig. 4(a) demonstrates the coexistence of κ_p and κ_c, which is closely related to the crystal-liquid duality discussed above. Upon heating, κ_p decreases following the T^{-1} decay of the Peierls' theory that accords with the calculated trend in Ref. 39, while κ_c slowly increases with temperature and meets κ_p in the vicinity of 650 K. As an addition to κ_L, κ_c strongly offsets the standard temperature dependence of Peierls-Boltzmann conductivity, leading the calculated temperature dependence being $\kappa_L \propto T^{-0.61}$ that agrees well with the experiment in Figs. 4(a) and S10. It works until experimentally observed κ_L in the shadow region appears to rise above 500 K due to the existence of bipolar thermal conduction and phase transitions.[35] In Fig. 4(b), we show the predominance of the population conductivity over the coherence conductivity with respect to the phonon frequency at 300 K. The population contribution of particlelike phonons originates mainly from the low-frequency modes below 10 meV, and other modes are insignificant. Meanwhile, all phonons contribute to the coherence term in the random distribution, which deviates from the conventional perspective that the acoustic modes are mainly responsible for heat transport in semiconductors.[59] The behaviors of these two terms result in the low-energy rapid growth of κ_p and the continuous increase in κ_c over the whole energy range in the insert of Fig. 4(b). As a consequence, κ_p and κ_c are calculated to be 0.45 and 0.19 $\mathrm{W\,m^{-1}\,K^{-1}}$, respectively, at 300 K. The κ_L of α-MgAgSb, as a sum of both κ_p and κ_c, is calculated to be 0.64 $\mathrm{W\,m^{-1}\,K^{-1}}$ at 300 K, which agrees with our measured room-temperature value of 0.63 $\mathrm{W\,m^{-1}\,K^{-1}}$.[39]

To analyze the strength of particlelike and wavelike conduction mechanisms, we resolve the phonon lifetime $\tau(\mathbf{q})_s$ as a function of the phonon energy E at different temperatures for α-MgAgSb. In Fig. 4(c), three regimes are divided in time by the Ioffe-Regel limit ($\tau_{\mathrm{Ioffe-Regel}} = 1/\omega$) and the Wigner limit ($\tau_{\mathrm{Wigner}} = 1/\Delta\omega_{\mathrm{avg}}$),[60,61] where the average phonon interband spacing, $\Delta\omega_{\mathrm{avg}} = \omega_{\mathrm{max}}/3N_a$, is defined as the ratio between the maximum phonon frequency (ω_{max}) and the number of phonon bands ($3N_a$). For these regimes, different heat conduction mechanisms work. We can see at 300 K phonons have lifetimes greater than $\tau_{\mathrm{Ioffe-Regel}}$ as the well-defined quasiparticle excitations describing the collective motions of atoms in the crystal. More specifically, phonons with large contributions to κ_L are greater than τ_{Wigner}, where heat predominantly transports in a particle-like manner. In addition, we should take note that there are lots of phonons at the intermediate region between $\tau_{\mathrm{Ioffe-Regel}}$ and τ_{Wigner} in the wavelike diffusion as in glasses. They are significant at 30% of the total κ_L at 300 K in α-MgAgSb. As a matter of fact, the κ_c in Fig. 4(b) can be decoupled in terms of the pairs of coupled modes (ω1, ω2), as shown in Fig. 4(d). Clearly, the major contributors to κ_c locate near the diagonal of the frequency plane with quasidegenerate vibrational frequencies, which is similar to the case of harmonic glasses.[61]

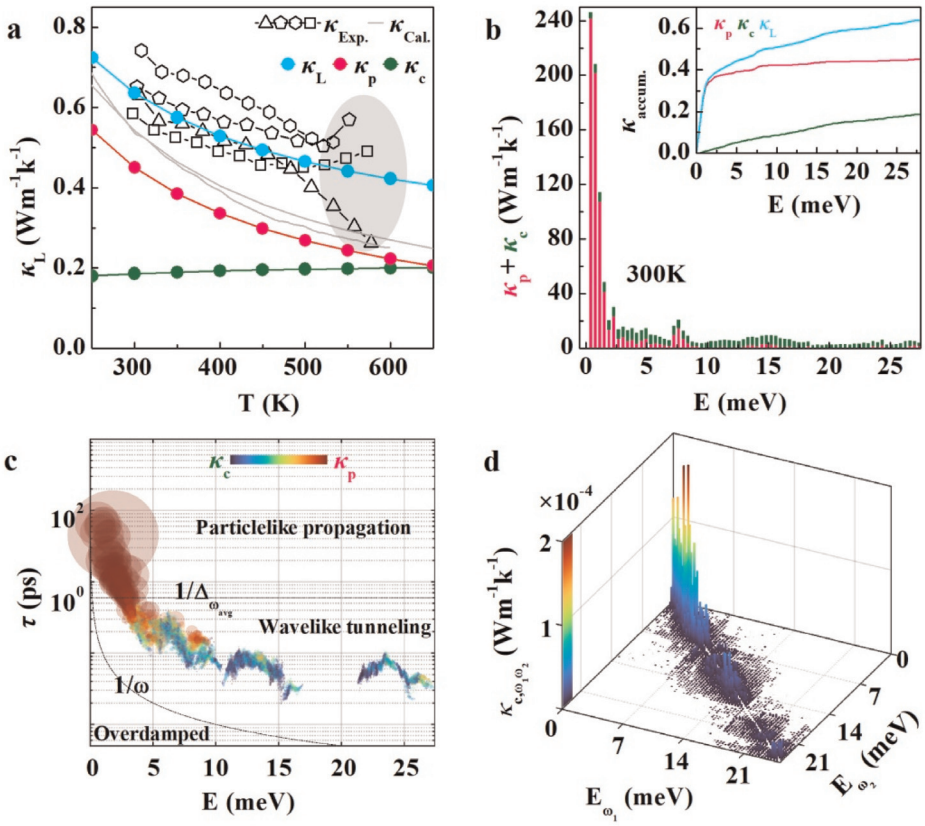

FIG. 4. Thermal properties of α-MgAgSb. (a) Measured temperature-dependent lattice thermal conductivity ($\kappa_{Exp.}$, black) and calculated values ($\kappa_L = \kappa_p + \kappa_c$). The triangle, pentagon, and hexagon indicate the κ_L for tantalum-sealing melted MgAgSb (sample 1), MgAgSb (sample 2), and carbon-coating melted MgAgSb, respectively, in Ref. 35, while the quadrangle represents the data extracted from our previous paper.[39] Gray lines are theoretical values from Refs. 39 and 40 calculated without temperature-induced frequency shifts and the coherence contributions. The experimental values of κ_L in the shadow region appear to rise above 500 K due to the existence of bipolar thermal conduction and phase transitions, which will not be discussed in this work. (b) Phonon-mode-resolved thermal conductivity of population (κ_p, pink) and coherence (κ_c, olive) contributions at 300 K. Inset: Cumulative total thermal conductivity (κ_L, cyan) as a sum of the population contribution (κ_p, pink) and coherence contribution (κ_c, olive) at 300 K. (c) Phonon lifetimes $\tau(\mathbf{q}) = [\Gamma(\mathbf{q})]^{-1}$ as a function of the energy for α-MgAgSb at 300 K. The area of each circle is proportional to the contribution to the κ_L and colored according to the origin of the contribution. (d) Two-dimensional density of states for the thermal conductivity, $\kappa_{c,\omega 1\omega 2}$, which resolves how much a Zener-like coupling between two vibrational modes having frequencies ω1ω2 contributes to the coherence conductivity.

V. CONCLUSIONS

In summary, we find that α-MgAgSb has the mixed part-crystalline part-liquid state and rattling-like thermal damping. On the basis of inelastic neutron scattering and theoretical calculations, we verify that α-MgAgSb holds low-energy localized phonon branches and avoided crossing of the rattler modes, dominated by the collective partially liquid-like motions of Ag atoms with large ADPs. By solving the two-channel thermal transport, we find that heat primarily transfers through particle-like propagation of phonon excitations, with a significant portion (around 30% at 300 K) from wavelike tunneling between different phonon states. Our study unveils that the synergistic effect of the soft crystalline sublattices and partially liquid-like motions of Ag atoms simultaneously lead to ultralow κ_L and abnormal temperature dependence of $\kappa_L \propto T^{-0.61}$ in α-MgAgSb. These fundamental insights regarding atomic dynamics shed new light on underlying the κ_L in complex crystalline compounds with intrinsic strong anharmonicity, which will facilitate the design of high-performance energy conversion materials.

VI. EXPERIMENTAL SECTION

Synthesis: We used a two-step process combining ball milling with hot pressing to synthesize the material α-$MgAg_{0.97}Sb_{0.99}$ as reported elsewhere.[33] For convenience, we denote α-$MgAg_{0.97}Sb_{0.99}$ as α-MgAgSb in our work.

Neutron diffraction measurements: The high-resolution neutron diffraction measurements were performed at 3 K using ECHIDNA[62] at the ANSTO, Australia. A Ge (331) monochromator was used to produce a monochromatic neutron beam of wavelength 2.4395 Å. The FullProf program was used for the Rietveld refinement with the α-MgAgSb tetragonal structure with a space group of $I\bar{4}C2$ (No. 120).

Inelastic neutron scattering measurements: Multi-E_i time-of-flight INS measurements were performed at the cold neutron disk chopper

spectrometer BL14 AMATERAS[63] at the J-PARC in Japan. The data with multiple neutron incident energies of 4.68, 7.74, and 42.00 meV are used.[64] A powder sample of 6.2518 g for α-$MgAg_{0.97}Sb_{0.99}$ was encased in a thin-walled aluminium cylinder. A top loading closed cycle refrigerator (TL-CCR) was used for the temperature-dependent measurements. The data collected at 300, 385, and 485 K were used. The data reduction was completed using UTSUSEMI version 0.3.6.[65] The resulting S(**Q**,E) was visualized in Mslice of the Data Analysis and Visualization Environment (DAVE).[66] It is a function of neutron energy transfer E and momentum transfer $\mathbf{Q} = \mathbf{k}_f - \mathbf{k}_i = \mathbf{q} + \tau$, where k_i (k_f) is the incident (scattered) neutron wave vector, **q** is the phonon wave vector, and τ is the reciprocal lattice vector. The Bose-factor-calibrated phonon DOS shown in Fig. 2(a) are the integration results with a integration **Q** region of 1.0–3.0 $Å^{-1}$.

Computational details: First-principles calculations were implemented in the Vienna *ab initio* simulation package (VASP),[67] within the framework of the Perdew–Burke–Ernzerhof[68] generalized gradient approximation.[69,70] The kinetic energy cutoff of plane wave was 500 eV on the 0.03 $Å^{-1}$ spacing Γ-centered k-mesh. All geometry structures were fully relaxed until the residual forces on each atom were less than 0.01 eV/Å. The second-order force constants were calculated within the harmonic approximation via the finite-displacement method[71] on a 5 × 5 × 5 k-mesh for α-MgAgSb. It was based on a 2 × 2 × 2 supercell (containing 192 atoms) by the Phonopy code[72] bundled with VASP.

The molecular dynamics calculations were performed with a 2 × 2 × 2 supercell via a canonical ensemble using a Nosè–Hoover thermostat. A total number of 50 ps with 1 fs time step at 300, 400, and 500 K, respectively, was calculated with a plane wave cutoff of 500 eV. The corrections to the second order force constants due to the finite temperature anharmonic effects were applied using the DynaPhoPy code[73] from molecular dynamics at the three different temperatures.

Third-order force constants were computed with the same settings in Refs. 39 and 40 Together with the Phono3py[74] package, the renormalized harmonic force constants from molecular dynamics and third-order force constants were Fourier interpolated on a convergent (12 × 12 × 12) grid for calculating the two-channel thermal conductivity, which include both the population and coherence contributions:[60,61] $\kappa_L = \kappa_p + \kappa_c$. The population term κ_p was the standard Peierls contribution to the conductivity. The additional tensor was named as κ_c (the coherence term) deriving from the off diagonal terms of the heat-flux operator, depicting the wavelike tunneling of coherent phonons. In Fig. S11 and S12, we show the convergence of κ_L with respect to Brillouin zone sampling density and temperature-dependent second order force constant. It shows our current calculations in the text are enough to give reliable results. Since α-MgAgSb belongs to the tetragonal system, it has anisotropic single-crystal κ parallel (κ_{xy}) and perpendicular (κ_z) to the xy plane in Fig. S12. In our work, the κ of polycrystalline sample is further averaged along the three principal crystallographic axes as compared to experimental values.

In order to compare with experimental data of the measured multi-E_i time-of-flight INS, the two-dimensional S(**Q**,E) patterns were calculated from the finite-temperature (300 K) harmonic force constants with the Euphonic package.[41] The neutron-weighted phonon density of states of α-MgAgSb was calculated by summing the atom-decomposed phonon density of states values weighted by the atomic scattering cross sections and masses,[39]

$$g_{tot}(\omega) = \sum_i f_i \frac{\sigma_i}{M_i} g_i(\omega),$$

where the sum over *i* includes all elements in the sample, f_i is the atomic concentration, σ_i is the total neutron cross section, M_i is the atomic mass, and $g_i(\omega)$ is the partial density of states of the element *i*.

SUPPLEMENTARY MATERIAL

See the supplementary material for crystal structures, neutron diffraction data, phonon dispersions, powder-averaged S(**Q**,E), atom displacement parameters, metavalent bonding map, velocity autocorrelation functions, self-part of van Hove correlation functions, fitting results of measured temperature-dependent lattice thermal conductivity, convergence test of calculated lattice thermal conductivity, and lattice parameters mentioned in the main text.

ACKNOWLEDGMENTS

P.F.L. acknowledges the financial support from the Guangdong Basic and Applied Basic Research Foundation (Grant No. 2022A1515140030) and the National Natural Science Foundation of China (Grant Nos. 12104458). Y.S.Z. acknowledges the financial support from the program of Distinguished Expert of Taishan Scholar (No. tstp20221124). F.W.W. acknowledges the financial support from the Science Center of the National Natural Science Foundation of China (Grant Nos. 52088101). The neutron scattering experiment at the Materials and Life Science Experimental Facility (MLF), J-PARC was performed under user program (AMATERAS proposal no. 2018A0061). The calculations were performed at the CSNS Scientific Computing Platform of Institute of High Energy Physics of CAS and GBA Sub-center of National HEP Science Data Center (CSNS SC Platform of IHEP CAS & GBA Sub-Center of NHEPDC).

AUTHOR DECLARATIONS

Conflict of Interest

The authors have no conflicts to disclose.

Author Contributions

Jingyu Li and Xiyang Li contributed equally to this work.

Jingyu Li: Conceptualization (equal); Data curation (equal); Formal analysis (equal); Investigation (equal); Methodology (equal); Visualization (equal); Writing – original draft (equal); Writing – review & editing (equal). **Jiehe Sui:** Supervision (equal); Validation (equal). **Huaizhou Zhao:** Supervision (equal); Validation (equal); Visualization (equal). **Fangwei Wang:** Project administration (equal); Supervision (equal); Writing – review & editing (equal). **Junrong Zhang:** Project administration (lead); Supervision (equal); Writing – original draft (equal); Writing – review & editing (equal). **Xiyang Li:** Conceptualization (equal); Data curation (equal); Investigation (equal); Validation (equal); Visualization (equal); Writing – original draft (equal). **Yongsheng Zhang:** Formal analysis (equal); Methodology (equal); Resources (equal); Supervision (equal). **Jianbo Zhu:** Conceptualization (equal); Formal analysis (equal); Methodology (equal); Software (equal). **Enyue Zhao:** Data curation (equal);

Methodology (equal); Validation (equal). **Maiko Kofu:** Data curation (equal); Methodology (equal); Validation (equal). **Kenji Nakajima:** Data curation (equal); Methodology (equal); Validation (equal). **Maxim Avdeev:** Data curation (equal); Methodology (equal); Validation (equal). **Peng-Fei Liu:** Conceptualization (equal); Data curation (equal); Formal analysis (equal); Funding acquisition (equal); Investigation (equal); Methodology (equal); Project administration (equal); Resources (equal); Software (equal); Supervision (equal); Validation (equal); Visualization (equal); Writing – original draft (equal); Writing – review & editing (equal).

DATA AVAILABILITY

The data that support the findings of this study are available from the corresponding authors upon reasonable request.

REFERENCES

[1]Q. Yan and M. G. Kanatzidis, Nat. Mater. **21**, 503 (2021).
[2]X.-L. Shi, J. Zou, and Z.-G. Chen, Chem. Rev. **120**, 7399 (2020).
[3]Y. Li, W. Li, T. Han, X. Zheng, J. Li, B. Li, S. Fan, and C.-W. Qiu, Nat. Rev. Mater. **6**, 488 (2021).
[4]L. Li, W.-D. Liu, Q. Liu, and Z.-G. Chen, Adv. Funct. Mater. **32**, 2200548 (2022).
[5]B. Qin, D. Wang, and L.-D. Zhao, InfoMat **3**, 755 (2021).
[6]M. Dutta, D. Sarkar, and K. Biswas, Chem. Commun. **57**, 4751 (2021).
[7]Z. Chen, X. Zhang, and Y. Pei, Adv. Mater **30**, 1705617 (2018).
[8]K. Biswas, J. He, I. D. Blum, C.-I. Wu, T. P. Hogan, D. N. Seidman, V. P. Dravid, and M. G. Kanatzidis, Nature **489**, 414 (2012).
[9]S. Roychowdhury, T. Ghosh, R. Arora, M. Samanta, L. Xie, N. K. Singh, A. Soni, J. He, U. V. Waghmare, and K. Biswas, Science **371**, 722 (2021).
[10]B. Jiang, Y. Yu, J. Cui, X. Liu, L. Xie, J. Liao, Q. Zhang, Y. Huang, S. Ning, B. Jia, B. Zhu, S. Bai, L. Chen, S. J. Pennycook, and J. He, Science **371**, 830 (2021).
[11]J. M. Hodges, S. Hao, J. A. Grovogui, X. Zhang, T. P. Bailey, X. Li, Z. Gan, Y.-Y. Hu, C. Uher, V. P. Dravid, C. Wolverton, and M. G. Kanatzidis, J. Am. Chem. Soc. **140**, 18115 (2018).
[12]G. Tan, F. Shi, S. Hao, H. Chi, T. P. Bailey, L.-D. Zhao, C. Uher, C. Wolverton, V. P. Dravid, and M. G. Kanatzidis, J. Am. Chem. Soc. **137**, 11507 (2015).
[13]M. K. Jana and K. Biswas, ACS Energy Lett. **3**, 1315 (2018).
[14]W. G. Zeier, A. Zevalkink, Z. M. Gibbs, G. Hautier, M. G. Kanatzidis, and G. J. Snyder, Angew. Chem. Int. Ed. **55**, 6826 (2016).
[15]G. S. Nolas, D. T. Morelli, and T. M. Tritt, Annu. Rev. Mater. Sci. **29**, 89 (1999).
[16]T. Takabatake, K. Suekuni, T. Nakayama, and E. Kaneshita, Rev. Mod. Phys. **86**, 669 (2014).
[17]K. Zhao, P. Qiu, X. Shi, and L. Chen, Adv. Funct. Mater. **30**, 1903867 (2019).
[18]H. Liu, X. Shi, F. Xu, L. Zhang, W. Zhang, L. Chen, Q. Li, C. Uher, T. Day, and G. J. Snyder, Nat. Mater **11**, 422 (2012).
[19]S. Mukhopadhyay, D. S. Parker, B. C. Sales, A. A. Puretzky, M. A. McGuire, and L. Lindsay, Science **360**, 1455 (2018).
[20]C. W. Li, J. Hong, A. F. May, D. Bansal, S. Chi, T. Hong, G. Ehlers, and O. Delaire, Nat. Phys. **11**, 1063 (2015).
[21]O. Delaire, J. Ma, K. Marty, A. F. May, M. A. McGuire, M.-H. Du, D. J. Singh, A. Podlesnyak, G. Ehlers, M. D. Lumsden, and B. C. Sales, Nat. Mater. **10**, 614 (2011).
[22]P. Acharyya, T. Ghosh, K. Pal, K. S. Rana, M. Dutta, D. Swain, M. Etter, A. Soni, U. V. Waghmare, and K. Biswas, Nat. Commun. **13**, 5053 (2022).
[23]J. He, Y. Xia, W. Lin, K. Pal, Y. Zhu, M. G. Kanatzidis, and C. Wolverton, Adv. Funct. Mater. **32**, 2108532 (2021).
[24]Y. Xia, D. Gaines, J. He, K. Pal, Z. Li, M. G. Kanatzidis, V. Ozoli, and C. Wolverton, Proc. Natl. Acad. Sci. U. S. A. **120**, e2302541120 (2023).
[25]D. Li, H. Zhao, S. Li, B. Wei, J. Shuai, C. Shi, X. Xi, P. Sun, S. Meng, L. Gu, Z. Ren, and X. Chen, Adv. Funct. Mater **25**, 6478 (2015).
[26]D. Kraemer, J. Sui, K. McEnaney, H. Zhao, Q. Jie, Z. F. Ren, and G. Chen, Energy Environ. Sci. **8**, 1299 (2015).
[27]Z. Liu, J. Mao, J. Sui, and Z. Ren, Energy Environ. Sci. **11**, 23 (2018).
[28]Z. Liu, Y. Wang, J. Mao, H. Geng, J. Shuai, Y. Wang, R. He, W. Cai, J. Sui, and Z. Ren, Adv. Energy Mater. **6**, 1502269 (2016).
[29]Z. Liu, H. Geng, J. Mao, J. Shuai, R. He, C. Wang, W. Cai, J. Sui, and Z. Ren, J. Mater. Chem. A **4**, 16834 (2016).
[30]Z. Liu, Y. Zhang, J. Mao, W. Gao, Y. Wang, J. Shuai, W. Cai, J. Sui, and Z. Ren, Acta Mater **128**, 227 (2017).
[31]X. Tan, L. Wang, H. Shao, S. Yue, J. Xu, G. Liu, H. Jiang, and J. Jiang, Adv. Energy Mater. **7**, 1700076 (2017).
[32]Z. Liu, W. Gao, X. Meng, X. Li, J. Mao, Y. Wang, J. Shuai, W. Cai, Z. Ren, and J. Sui, Scr. Mater. **127**, 72 (2017).
[33]H. Zhao, J. Sui, Z. Tang, Y. Lan, Q. Jie, D. Kraemer, K. McEnaney, A. Guloy, G. Chen, and Z. Ren, Nano Energy **7**, 97 (2014).
[34]P. Ying, X. Liu, C. Fu, X. Yue, H. Xie, X. Zhao, W. Zhang, and T. Zhu, Chem. Mater. **27**, 909 (2015).
[35]Y. Huang, J. Lei, H. Chen, Z. Zhou, H. Dong, S. Yang, H. Gao, T.-R. Wei, K. Zhao, and X. Shi, Acta Mater. **249**, 118847 (2023).
[36]L. Xie, J. Yang, Z. Liu, N. Qu, X. Dong, J. Zhu, W. Shi, H. Wu, G. Peng, F. Guo, Y. Zhang, W. Cai, H. Wu, H. Zhu, H. Zhao, Z. Liu, and J. Sui, Mater. Today **65**, 5 (2023).
[37]J. Zhu, L. Xie, Z. Ti, J. Li, M. Guo, X. Zhang, P.-F. Liu, L. Tao, Z. Liu, Y. Zhang, and J. Sui, Appl. Phys. Rev. **10**, 031405 (2023).
[38]L. Xie, L. Yin, Y. Yu, G. Peng, S. Song, P. Ying, S. Cai, Y. Sun, W. Shi, H. Wu, N. Qu, F. Guo, W. Cai, H. Wu, Q. Zhang, K. Nielsch, Z. Ren, Z. Liu, and J. Sui, Science **382**, 921–928 (2023).
[39]X. Li, P.-F. Liu, E. Zhao, Z. Zhang, T. Guidi, M. D. Le, M. Avdeev, K. Ikeda, T. Otomo, M. Kofu, K. Nakajima, J. Chen, L. He, Y. Ren, X.-L. Wang, B.-T. Wang, Z. Ren, H. Zhao, and F. Wang, Nat. Commun. **11**, 942 (2020).
[40]J.-Y. Yang, W. Zhang, and M. Hu, J. Appl. Phys. **125**, 205105 (2019).
[41]R. Fair, A. Jackson, D. Voneshen, D. Jochym, D. Le, K. Refson, and T. Perring, J. Appl. Crystallogr. **55**, 1689 (2022).
[42]M. Christensen, A. B. Abrahamsen, N. B. Christensen, F. Juranyi, N. H. Andersen, K. Lefmann, J. Andreasson, C. R. H. Bahl, and B. B. Iversen, Nat. Mater. **7**, 811–815 (2008).
[43]S. Han, S. Dai, J. Ma, Q. Ren, C. Hu, Z. Gao, M. Duc Le, D. Sheptyakov, P. Miao, S. Torii, T. Kamiyama, C. Felser, J. Yang, C. Fu, and T. Zhu, Nat. Phys. **19**, 1649–1657 (2023).
[44]C. H. Lee, I. Hase, H. Sugawara, H. Yoshizawa, and H. Sato, J. Phys. Soc. Jpn. **75**, 123602 (2006).
[45]R. P. Hermann, R. Jin, W. Schweika, F. Grandjean, D. Mandrus, B. C. Sales, and G. J. Long, Phys. Rev. Lett. **90**, 135505 (2003).
[46]P. Ying, X. Li, Y. Wang, J. Yang, C. Fu, W. Zhang, X. Zhao, and T. Zhu, Adv. Funct. Mater. **27**, 1604145 (2016).
[47]J.-L. Mi, P.-J. Ying, M. Sist, H. Reardon, P. Zhang, T.-J. Zhu, X.-B. Zhao, and B. B. Iversen, Chem. Mater. **29**, 6378 (2017).
[48]W. Qiu, L. Xi, P. Wei, X. Ke, J. Yang, and W. Zhang, Proc. Natl. Acad. Sci. U. S. A. **111**, 15031 (2014).
[49]J.-Y. Raty, M. Schumacher, P. Golub, V. L. Deringer, C. Gatti, and M. Wuttig, Adv. Mater. **31**, 1806280 (2018).
[50]A. Zaccone and M. Baggioli, Proc. Natl. Acad. Sci. U. S. A. **118**, e2022303118 (2021).
[51]Y. Zhou, S. Xiong, X. Zhang, S. Volz, and M. Hu, Nat. Commun. **9**, 4712 (2018).
[52]N. K. Tailor and S. Satapathi, Scr. Mater. **223**, 115061 (2023).
[53]K. Miyata, T. L. Atallah, and X.-Y. Zhu, Sci. Adv. **3**, e1701469 (2017).
[54]P. R. Okamoto, N. Q. Lam, and L. E. Rehn, Solid State Phys. **52**, 1–135 (1999).
[55]L. Van Hove, Phys. Rev. **95**, 249 (1954).
[56]L. Xie, D. Wu, H. Yang, Y. Yu, Y. Wang, and J. He, J. Mater. Chem. C **7**, 9263 (2019).
[57]B. Li, H. Wang, Y. Kawakita, Q. Zhang, M. Feygenson, H. L. Yu, D. Wu, K. Ohara, T. Kikuchi, K. Shibata, T. Yamada, X. K. Ning, Y. Chen, J. Q. He, D. Vaknin, R. Q. Wu, K. Nakajima, and M. G. Kanatzidis, Nat. Mater. **17**, 226 (2018).
[58]S. Lin, W. Li, and Y. Pei, Mater. Today **48**, 198 (2021).
[59]P.-F. Liu, T. Bo, J. Xu, W. Yin, J. Zhang, F. Wang, O. Eriksson, and B.-T. Wang, Phys. Rev. B **98**, 235426 (2018).
[60]M. Simoncelli, N. Marzari, and F. Mauri, Nat. Phys. **15**, 809 (2019).
[61]M. Simoncelli, N. Marzari, and F. Mauri, Phys. Rev. X **12**, 041011 (2022).
[62]M. Avdeev and J. R. Hester, J. Appl. Cryst. **51**, 1597 (2018).

[63]K. Nakajima, S. Ohira-Kawamura, T. Kikuchi, M. Nakamura, R. Kajimoto, Y. Inamura, N. Takahashi, K. Aizawa, K. Suzuya, K. Shibata, T. Nakatani, K. Soyama, R. Maruyama, H. Tanaka, W. Kambara, T. Iwahashi, Y. Itoh, T. Osakabe, S. Wakimoto, K. Kakurai, F. Maekawa, M. Harada, K. Oikawa, R. E. Lechner, F. Mezei, and M. Arai, J. Phys. Soc. Jpn. **80**, SB028 (2011).
[64]M. Nakamura, R. Kajimoto, Y. Inamura, F. Mizuno, M. Fujita, T. Yokoo, and M. Arai, J. Phys. Soc. Jpn. **78**, 093002 (2009).
[65]Y. Inamura, T. Nakatani, J. Suzuki, and T. Otomo, J. Phys. Soc. Jpn. **82**, SA031 (2013).
[66]R. T. Azuah, L. R. Kneller, Y. Qiu, P. L. W. Tregenna-Piggott, C. M. Brown, J. R. D. Copley, and R. M. Dimeo, J. Res. Natl. Inst. Stand. Technol. **114**, 341 (2009).
[67]G. Kresse and J. Furthmuller,¨Phys. Rev. B **54**, 11169 (1996).
[68]G. Kresse and D. Joubert, Phys. Rev. B **59**, 1758 (1999).
[69]P. E. Blochl,¨Phys. Rev. B **50**, 17953 (1994).
[70]P. E. Blochl, O. Jepsen, and O. K. Andersen, ¨ Phys. Rev. B **49**, 16223 (1994).
[71]S. Baroni, S. de Gironcoli, A. Dal Corso, and P. Giannozzi, Rev. Mod. Phys. **73**, 515 (2001).
[72]A. Togo, F. Oba, and I. Tanaka, Phys. Rev. B **78**, 134106 (2008).
[73]A. Carreras, A. Togo, and I. Tanaka, Comput. Phys. Commun. **221**, 221 (2017).
[74]A. Togo, L. Chaput, and I. Tanaka, Phys. Rev. B **91**, 094306 (2015).